ACS Photonics

pubs.acs.org/journal/apchd5

Article

Understanding the Origin of Light Intensity and Temperature Dependence of Photodetection Properties in a $MAPbBr_3$ Single-Crystal-Based Photoconductor

Apurba Mahapatra, Vishnu Anilkumar, Rohit D. Chavan, Pankaj Yadav, and Daniel Prochowicz*

Cite This: *ACS Photonics* 2023, 10, 1424–1433

Read Online

ACCESS | Metrics & More | Article Recommendations | Supporting Information

ABSTRACT: Methylammonium lead bromide ($MAPbBr_3$), which belongs to the larger material family of lead halide perovskites (LHPs), has emerged as a promising semiconductor for the fabrication of single-crystal (SC)-based photodetectors (PDs). However, there is still a lack of sufficient understanding of the effect of irradiation power and applied temperature on the photodetection performance of SC-based perovskite PDs. Here, we investigate the impact of different light intensities and temperatures on the photodetection properties of planar-type $MAPbBr_3$ SC-based PD with the help of transient photoresponse and impedance spectroscopy. The light intensity-dependent study revealed that the key performance parameters of PD decrease with increasing irradiation intensity due to changes in charge recombination and carrier lifetime. On the other hand, the detrimental effect of increasing temperature on the performance of PD was found to be related to the ion accumulation, increasing scattering of impurities and phonons, and change in conductivity and band gap rather than the change in charge recombination. This study provides a thorough understanding of the origin of light intensity and temperature-dependent photodetection properties of SC-based PD, which is crucial for the further advancement of optoelectronic devices based on LHPs.

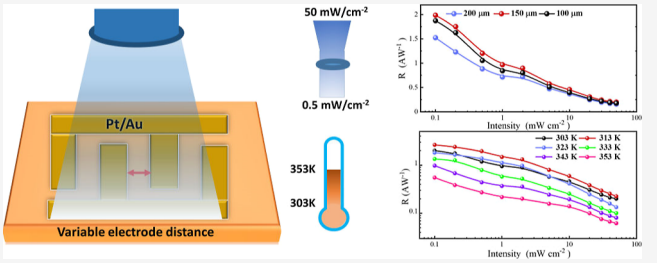

KEYWORDS: *lead halide perovskite, single crystal, photodetector, transient photoresponse impedance spectroscopy*

1. INTRODUCTION

Photodetectors (PDs) are a type of optoelectronic devices used to detect different lights and convert them into detectable electrical current. Fundamentally speaking, an illuminated semiconductor material absorbs the incident photons and generates electron–hole pairs, which are then separated, collected, and transferred to an external circuitry by an electric field. To be a sensitive and fast PD, a semiconductor material should possess a high absorption extinction coefficient, large charge carrier mobility, and low density of defects.[1] Nowadays, commercial PDs are based on inorganic semiconductors like silicon, germanium, and indium gallium arsenide (InGaAs), which are widely used in environmental monitoring, optical communication, and sensing.[2−6] However, processing this type of PDs requires very high temperature and expensive growth facilities, which limits their versatility toward broad eco-friendly applications and flexible electronics. Recently, lead halide perovskites (LHPs) have emerged as a new class of semiconductors for photodetection due to their solution processability, band gap tunability, and outstanding optoelectronic properties.[7−9] These materials can be easily obtained in the form of polycrystalline thin films[10] and single crystals (SCs).[11] Particularly, LHPs in the form of SCs reveal longer carrier diffusion length,[12] lower trap density, high charge mobility, and improved environmental stability[13] than their thin-film counterparts. Therefore, with the insignificant effect of grain boundary defects and surface defects, 2D and 3D LHP SCs hold huge promise for photodetection.[14−19]

Photoconductors are the most widely adopted device architecture for LHP SCs, which can be achieved by depositing two metal contacts separated with a channel on one plane of a SC. A prime example of a LHP SC for a photoconductor is methylammonium lead bromide ($MAPbBr_3$), which shows a wide detection range from visible to X-ray region with outstanding perfomance.[20−24] For example, Liu et al. grew high-quality $MAPbBr_3$ SCs using a low-temperature-gradient crystallization process and fabricated a PD with high responsivity (R = 16 A W^{-1}) and specific detectivity (D^* = 6×10^{13} Jones) of the green light (515 nm) due to very low trap density, longer carrier diffusion length, and high carrier mobility.[21,25] In other work, Cho et al. reported the low dissolution temperature growth technique of $MAPbBr_3$ SCs,

Received: January 6, 2023
Published: April 5, 2023

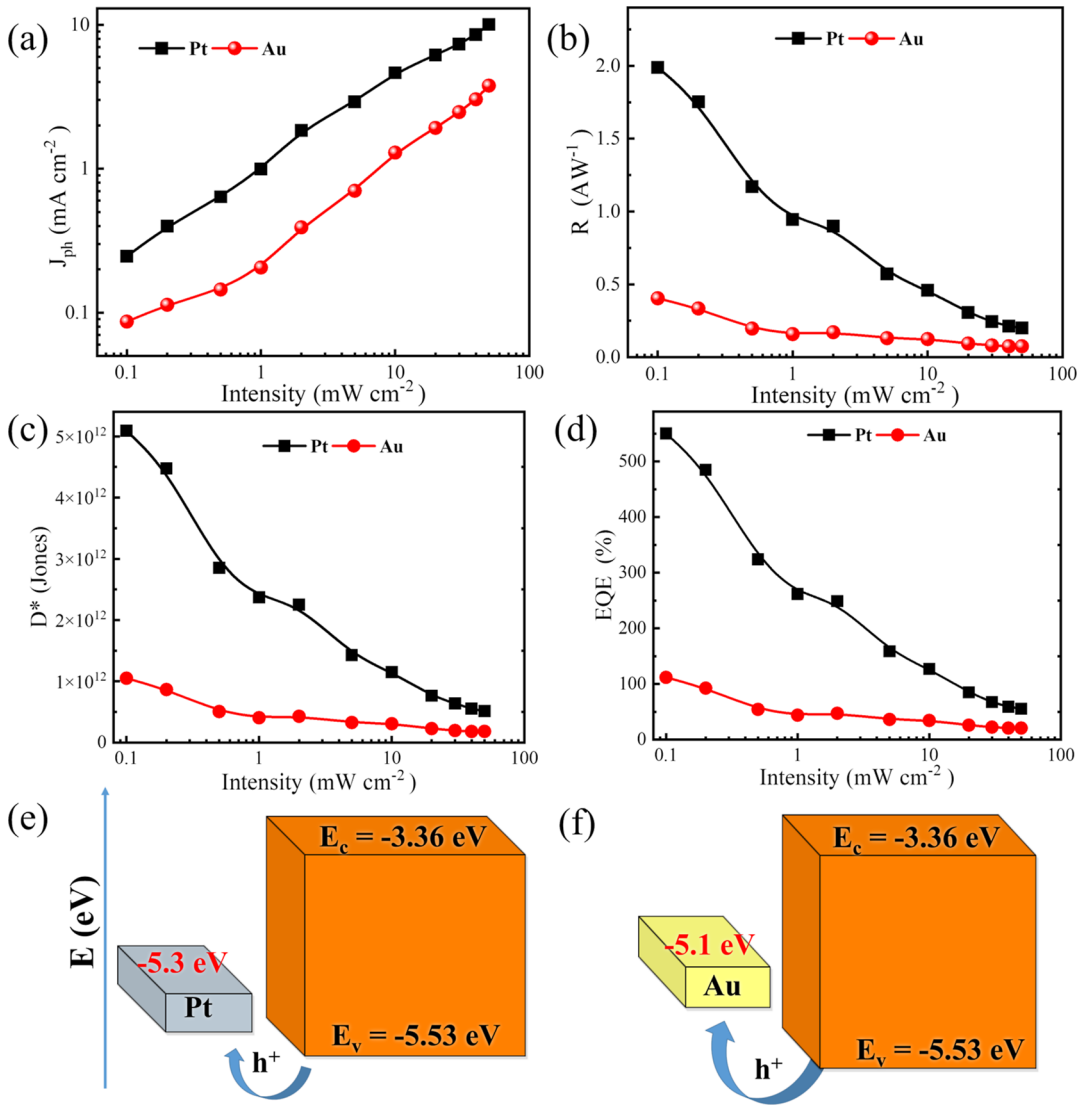

Figure 1. (a) Photocurrent density (J_{ph}), (b) responsivity (R), (c) specific detectivity (D^*), and (d) EQE of the fabricated planar-type $MAPbBr_3$ SC-based PDs with Pt and Au electrodes under blue LED light (λ = 448 nm). Energy band diagram of the planar-type $MAPbBr_3$ SC-based PD with (e) Pt and (f) Au electrodes.

which shows the potential in the white light photodetection.[26] Furthermore, the PD based on the $MAPbBr_3$ SC can exhibit the facet-dependent electrical properties, leading to different photodetection performances on (111) and (100) facet devices.[22,27] Notably, the above-mentioned works demonstrated the photodetection ability of the $MAPbBr_3$ SC-based PD at only room temperature. Although the temperature dependence current−voltage studies of various LHP SCs in the dark have been recently reported,[13,28−31] the temperature-dependent operational behavior of SC-based perovskite PDs has been rarely studied. Moreover, to the best of our knowledge, there is no study that explains the effect of different light intensities and temperatures on the output performance of SC-based perovskite PDs with the help of impedance spectroscopy (IS).

Here, we systematically investigated the effect of different light intensities and temperatures on the photodetection properties and impedance response characteristics of a planar-type $MAPbBr_3$ SC-based PD. First, we optimize the photodetection performance of our PD by selecting the proper metal electrode and its electrode spacing. We found that the $MAPbBr_3$ SC-based PD with a platinum (Pt) electrode and an electrode spacing of 150 μm exhibits the best output performance. Further light intensity-dependent study reveals that the decreased performance of our PD with increasing light intensity is due to the increased charge recombination and change in the carrier lifetime. In turn, the temperature-dependent PD performances are found to be related to the combined effect of ion accumulation, increasing scattering of impurities and phonons, conductivity, and band gap at higher temperatures.

2. RESULTS AND DISCUSSION

2.1. Selection of a Proper Electrode for PD Characterization. $MAPbBr_3$ SCs with a dimension of ca. 4 × 4 × 2 mm^3 were selected for the fabrication of planar-structured PDs by depositing the metal electrode on the surface of the crystal (for synthesis details and device fabrication, see the Experimental Section). The cubic perovskite structure was confirmed by powder X-ray diffraction (XRD) analysis of the grounded $MAPbBr_3$ crystals (Figure S1). The proper selection of metal contact plays an important role in the photoconductor-type

https://doi.org/10.1021/acsphotonics.3c00033
ACS Photonics 2023, 10, 1424−1433

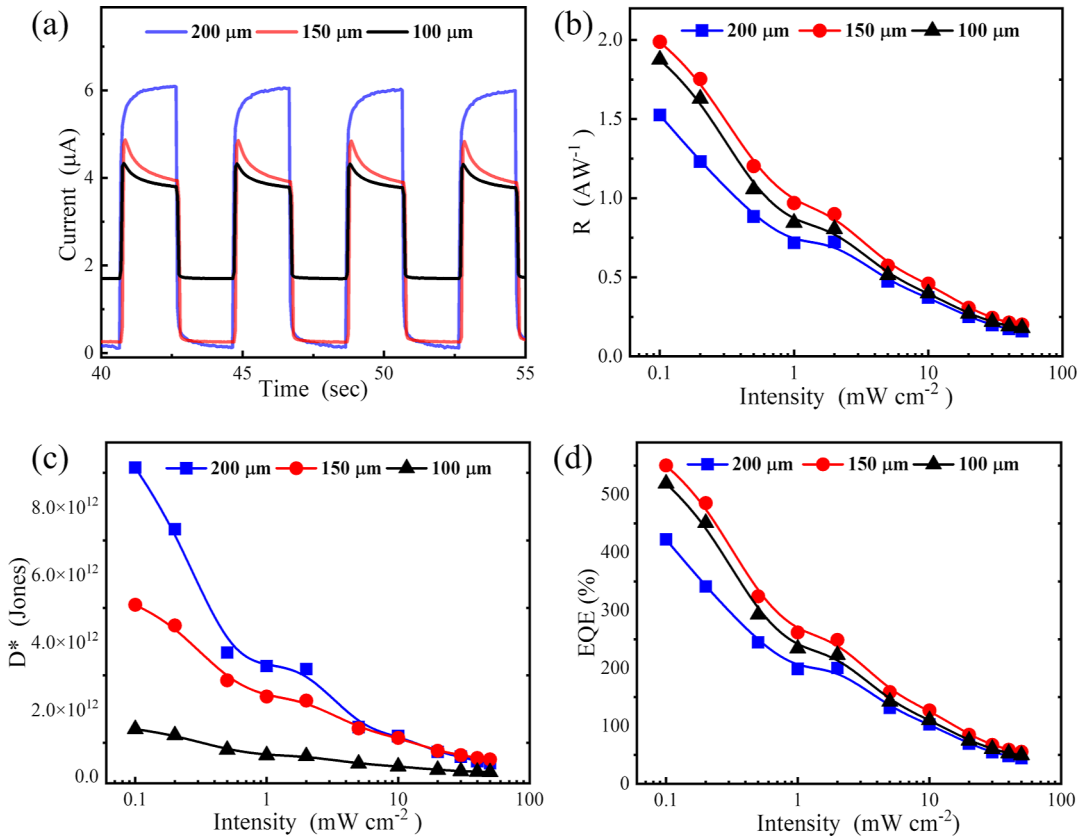

Figure 2. (a) Current−time (I−t) characteristics of PDs at 0.5 mW cm^{-2} irradiance power. (b) Responsivity (R), (c) specific detectivity (D*), and (d) EQE of fabricated $MAPbBr_3$ SC-based PDs with variable Pt electrode spacing (100, 150, and 200 μm).

PD due to the formation of a Schottky junction between the perovskite semiconductor and the metal electrode. The performance of this device is found to be mainly influenced by the quality of the SC and the Schottky barrier height (Φ_{SB}, SBH) between the metal and the semiconductor, which describes the energy barrier for the charge carriers to pass through the contact.[14,32,33]

In this work, we study the effect of gold (Au) and platinum (Pt) electrodes on the photodetection properties of the $MAPbBr_3$ SC. The schematic representation of the fabricated PD is shown in Figure S2. Figure S3 shows the transient photoresponses of the $MAPbBr_3$ PDs with Au and Pt electrodes, which were measured at a fixed bias voltage of 2 V and under blue LED (λ = 448 nm) light pulse with irradiance power densities ranging from 0.1 to 50 mW cm^{-2}. The applied bias was chosen based on the typical photocurrent−voltage (I_{ph}−V) curves (Figure S4a) and chopped-light current−voltage characteristics (Figure S4b). From these curves, we can observe that I_{ph} increases with applied bias and slows down after exceeding 2 V. In addition, both the PDs exhibit uniform current transient response around 2 V. The photocurrent as a function of incident light intensity for both the PDs is shown in Figure 1a. As can be seen, the photocurrent increases with increasing the intensity of incident light due to the increase in charge generation rate. Notably, the $MAPbBr_3$ PD with the Pt electrode generates almost 2 times higher I_{ph} than the Au-based $MAPbBr_3$ PD, which suggests its superior performance. We therefore proceeded to a complete performance metrics of both the PDs. The observed dark currents for the $MAPbBr_3$ PD with Pt and Au electrodes are almost similar and equal to 249 and 245 nA, respectively. The responsivity (R), which represents the photoresponse to the incident light, was calculated using the equation

$$R = (J_{ph} - J_d)/P$$

where J_{ph} is the photocurrent density, J_d is the dark current density, and P is the input illumination power density. The specific detectivity (D*), which represents the performance of the PD, can be calculated by using the equation

$$D^* = R/\sqrt{(2qJ_d)}$$

From Figure 1b,c, we can observe that the Pt-based $MAPbBr_3$ PD exhibits almost 5 times higher responsivity (R) and specific detectivity (D*) than the Au-based $MAPbBr_3$ PD. The maximum R and D* increases to 1.99 A W^{-1} and 5.09 × 10^{12} Jones for the Pt-based $MAPbBr_3$ PD as compared to the Au-based $MAPbBr_3$ PD (0.41 A W^{-1} and 1.05 × 10^{12} Jones) under 0.1 mW cm^{-2} blue light. The external quantum efficiency (EQE) of both the PDs is calculated by using the equation

$$EQE = Rhc/e\lambda$$

where h is Planck's constant, c is the speed of light, e is the charge of electron, and λ is the wavelength of the incident light. It was found that the Pt-based $MAPbBr_3$ PD shows almost 6 times higher EQE compared to the Au-based $MAPbBr_3$ PD (Figure 1d).

The collection of photogenerated charge carriers strongly depends on the charge collection grid pattern, charge separation, and recombination. In our previous study,[33] we demonstrated that the performance of the SC-based PD is

https://doi.org/10.1021/acsphotonics.3c00033
ACS Photonics 2023, 10, 1424−1433

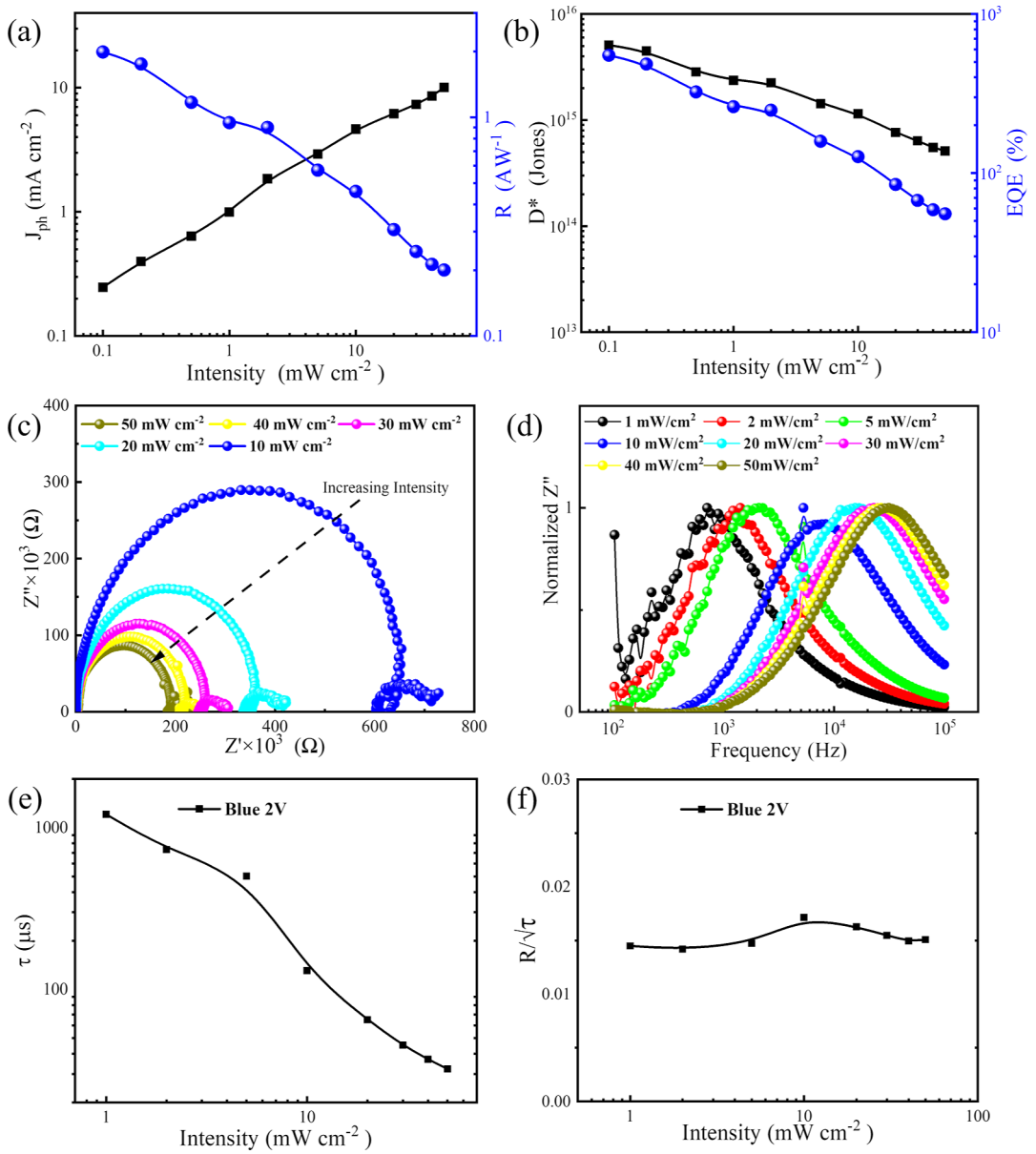

Figure 3. (a) Logarithmic photocurrent density and responsivity and (b) specific detectivity and external quantum efficiency as a function of irradiation intensity at 303 K. (c) Nyquist spectra and (d) normalized imaginary part of IS spectra versus frequency under various irradiation power at 303 K. (e) Carrier recombination lifetime and (f) $R/\sqrt{\tau}$ of a PD under various irradiation intensities of blue light at 2 V.

affected by the change in SBH between the metal and the semiconductor. In other work, Gavranovic et al. reported that the Fermi-level (E_{f0}) of $MAPbBr_3$ changes with changing the electrode spacing, influencing the SBH between the metal and the semiconductor.[34] We noted that in our case, there is no change in the Fermi level of $MAPbBr_3$ due to the use of Pt and Au electrodes with the same electrode spacing (150 μm). Moreover, we used $MAPbBr_3$ SCs from the same batch to minimize the effect of crystal quality on the Fermi level of $MAPbBr_3$ SCs. Therefore, the SBH between the metal and $MAPbBr_3$ is only influenced by the change of band structure of the electrode contact. Figure 1e,f shows the band diagram of $MAPbBr_3$ with Pt and Au electrodes with energy levels derived from the literature.[14,33,34] As can be seen, the Pt electrode shows better SBH alignment with $MAPbBr_3$ than the Au electrode, which should lead to better charge extraction and consequently PD performance. To verify the quality of the synthesized SCs, we fabricated Au/$MAPbBr_3$/Au and Pt/$MAPbBr_3$/Pt devices with the vertical geometry and calculated their trap densities (η_h) and carrier mobilities by the space charge-limited current (SCLC) method (Figure S5). The values of trap density and carrier mobility for Pt/$MAPbBr_3$/Pt and Au/$MAPbBr_3$/Au devices are found to be similar and equal to 2.27 × 10^9 cm^{-3} and 34 cm^2 V^{-1} s^{-1}, and 2.23 × 10^9 cm^{-3} and 27 cm^2 V^{-1} s^{-1}, respectively. These results are comparable with the previously reported works.[21,22,27,34]

2.2. Effect of Electrode Spacing for PD Performance.

As the Pt electrode shows better SBH alignment with $MAPbBr_3$, we fabricate a set of planar-type $MAPbBr_3$ SC-based PDs with electrode spacings of 100, 150, and 200 μm. The transient photoresponses of a PD with different electrode spacings were measured at a fixed bias voltage of 2 V under blue LED (λ = 448 nm) light pulse with irradiance power densities ranging from 0.1 to 50 mW cm^{-2} (Figure S6). The

https://doi.org/10.1021/acsphotonics.3c00033
ACS Photonics 2023, 10, 1424−1433

current−time (I−t) characteristics of PDs at 0.5 mW cm^{-2} irradiance power are shown in Figure 2a. As can be seen, the photocurrent increases with increasing electrode spacing due to the increase in active area. In turn, the values of J_{ph} rise with decreasing electrode spacing (Figure S7a). The noise signals and dark currents for the fabricated $MAPbBr_3$ SC-based PDs are shown in Figure S7b. On the other hand, with increasing of the electrode spacing, a decrease in the dark current is observed due to the change of the effective electric field under different electrode spacings. The effective electric field decreases with increasing of the electrode spacing, leading to lower dark current of the PD, which is beneficial for better detectivity.[34] From Figure 2a, we can also observe that the photocurrent decreases with time after reaching the maximum for the devices with 100 and 150 μm electrode spacing. However, for the device with a 200 μm electrode spacing, the photocurrent increases gradually until it reaches a saturation. The change in photocurrent shape in the I−t plot for the SC-based PDs has also been observed by others.[14,34−36] For example, Cho et al. demonstrated that the variation of photocurrent shape can be related to the changeable dominating factor from carrier trapping at the defect states to carrier recombination under the different illumination conditions.[35] However, the mechanism underlying the change in photocurrent shape with changing the electrode spacing is still unclear and need further investigation.

To further investigate the PD properties, we determined the performance metrics of each device at different irradiations ranging from 0.1 to 50 mW cm^{-2}. The device parameters were calculated and plotted against the various irradiation power of incident light (Figure 2b−d). The maximum responsivity (R), specific detectivity (D^*), and EQE for a device with 100 μm Pt electrode spacing are estimated to be 1.88 A W^{-1}, D^* of 1.41 × 10^{12} Jones, and 519% under 0.1 mW cm^{-2} blue light at a fixed bias voltage of 2 V. At the same condition, the device with 150 μm Pt electrode spacing exhibits the R of 1.99 A W^{-1}, D^* of 5.09 × 10^{12} Jones, and EQE of 553%, which corresponds to an ∼10% increase compared to the device with 100 μm Pt electrode spacing. However, the R and EQE for the device with 200 μm Pt electrode spacing decreased and equals to 1.53 and 422%, respectively. The estimated values of rise time (from 10 to 90% of the saturated values) and fall time (from 90 to 10% of the saturated values) for all PDs are summarized in Table S1. As expected, the device with 150 μm Pt electrode spacing shows the fastest response speed and rise and fall time. For the device with 200 μm Pt electrode spacing, the performance and speed of the PD decreases due to the combination effect of increase in charge recombination and inefficient collection of the generated charges. The probability of these processes increases with increasing of the distance for charge carrier transport between the symmetrical contacts. On the other hand, D^* increases with increasing of the electrode spacing due to the decrease in dark current. Thus, the highest D^* (9.16 × 10^{12} Jones) is observed for the device with 200 μm Pt electrode spacing under 0.1 mW cm^{-2} irradiation of blue light.

2.3. Light Intensity and Temperature-Dependent PD Performance. The stable and consistent performance of a PD over a wide light intensity range is essential for most of the photodetection applications.[14,37,38] As can be seen in Figure 2a, the device with 150 μm electrode spacing exhibits uniform photoresponse with attractive performance metric values under the fast optical signals compared to the device with 100 and 200 μm electrode spacings. In contrast, the performance of the $MAPbBr_3$ SC-based PD with the Au electrode increases with decreasing of the electrode spacing, which is consistent with the previously reported study.[34] As shown in Figure S8, the device with 100 μm Au electrode spacing exhibits an R value of 0.58 A W^{-1} under 0.1 mW cm^{-1} irradiation intensity, which is much lower than the R value of the device with 150 μm Pt electrode spacing. Thus, the device with 150 μm Pt electrode spacing was chosen to further study the effect of different intensities and temperatures on its performance.

The functional stability of the investigated device is shown in Figure S9. The output of this PD is stable (∼90% performance remaining after 24 h of continuous operation under 1 mW cm^{-2} optical signal), and it is comparable with the previous studies.[21,25,34] Figure 3a shows the logarithmic plot of J_{ph} and R of a PD as a function of the irradiation intensity. The fitting of the results with a power law ($J_{ph} \propto P^{\beta}$, where P is the irradiation power and β is the recombination under illumination) shows a sublinear relationship between J_{ph} and irradiation power (Figure S10). This plot is a reflection of complex photoelectric processes within the spacing between two electrodes, which is controlled by the SBH alignment, quality of the crystal, different types of recombination, and charge transport properties of the material.[9,39] In general, the power exponent β equals to 1 or is very close to 1 for a high-performance PD.[40] However, a nonunity exponent of β ($0 < \beta < 1$) is often found in LHP-based PDs due to the existence of complex processes of carrier generation, charge trapping, and charge recombination within the absorber material.[40] In our case, the obtained value of β (0.6 ± 0.01) suggests the existence of second-order charge recombination, which dominates during the photodetection process.[12]

The performance parameters (R, D^*, and EQE) decrease linearly with increasing of the light intensity (Figure 3a,b). To shed more light on the charge recombination in our PD, intensity-dependent alternating current (AC) IS was carried out in frequencies ranging from 100 mHz to 1 MHz under irradiation power densities ranging from 0.1 to 50 mW cm^{-2}. In addition, a 2 V constant DC bias was applied during the IS measurement with 20 mV perturbation. The intensity-dependent impedance responses in the form of Nyquist plots are shown in Figures 3c and S11. The shape of the Nyquist plot appears as a semicircle at high frequencies, followed by a small inductive loop at intermediate frequencies and a semicircle at low frequencies. It is well established in perovskite-based devices (e.g., solar cells, LED) that the arc at low frequencies is related to the slow process of ion accumulation or migration,[13,14,41,42] while the arc at high frequencies is associated with the recombination process.[42−44] In turn, the inductive loop in IS can be associated with the complex multistep dynamics and mainly influence the surface states.[45,46] Recently, Guerrero et al. discussed the role of inductive loop for the high performing solar cells and poorly performing solar cells fabricated without selective contacts.[45] It was demonstrated that the absence/presence of an inductive feature in IS is directly related to the existence/lack of charge accumulation at the perovskite/contact interface. Therefore, the presence of the inductor loop in our PD could indicate the efficient charge separation due to the lack of charge accumulation at the perovskite/Pt interface. In addition, the arc at the high-frequency semicircle radius of the IS spectra is decreasing with increasing of the irradiation power, which is assigned to the recombination process of the PD. Because the number of photogenerated charges increases with increasing of the

https://doi.org/10.1021/acsphotonics.3c00033
ACS Photonics 2023, 10, 1424−1433

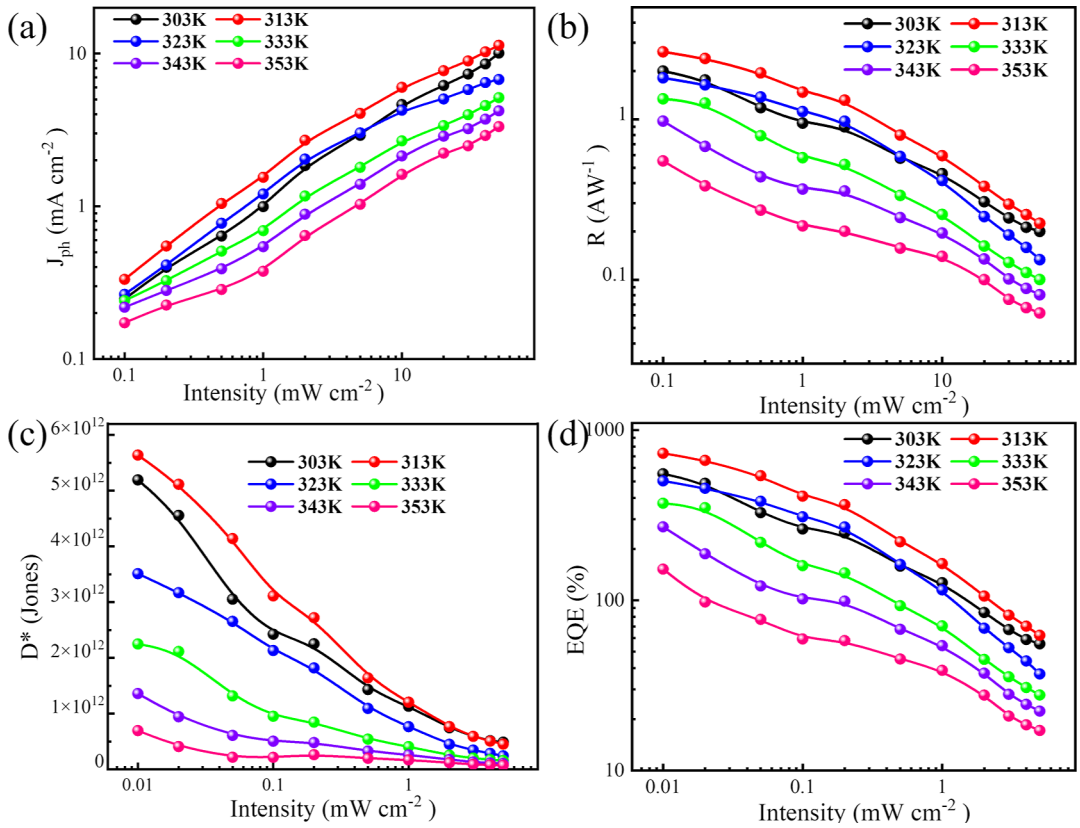

Figure 4. Temperature dependence (a) photocurrent density (J_{ph}), (b) responsivity (R), (c) specific detectivity (D^*), and (d) EQE of the $MAPbBr_3$ SC-based PD at different irradiation intensities.

irradiation power, the resistance of our PD reduces. In the case of low-frequency region, the semicircle radius decreases with increasing of the irradiation power due to the increase in ionic transport at higher irradiation intensities.[47,48] The irradiation dependence imaginary part of the complex impedance versus frequency is shown in Figure S12. As can be seen, the values of the imaginary part of complex impedance decreases with increasing of the irradiation power, which can be related to the low-frequency capacitance. Photoinduced ion migration increases with the increasing of the irradiation intensity, and these ions accumulate between the electrode and the $MAPbBr_3$ SC surface. Therefore, the values of low-frequency capacitance decreased at higher irradiation intensities. Figure 3d shows the normalized imaginary part of IS vs frequency as a function of irradiation power. The observed shift in the resonance frequency (f_0) toward the higher frequency range with increasing of the irradiation power indicates that the change is carrier recombination lifetime (τ).[12] As shown in Figure 3e, the value of τ calculated from the resonance frequency ($\tau = 1/f_0$) decreases with increasing of the irradiation power. This indicates the decrease in carrier diffusion length (L_D), which affects the efficient extraction of photogenerated charge carriers due to an increase in recombination.[49] In addition, the carrier mobility (μ) of a perovskite SC plays a vital role in the device properties. Thus, we were interested to study whether the value of R is related to μ under variable irradiation power. It is well known that the L_D depends on μ and τ, and it can be determined by the equation $L_D = (k_B T\mu\tau/e)^{1/2}$, where, e, k_B, and T are the elementary charge, Boltzmann constant, and absolute temperature, respectively.[12] Additionally, L_D is directly related to the device responsivity as $L_n + L_p = \frac{J_{SC}}{eG} = \frac{J_{SC}}{P} = R$, where G, L_n, and L_p are the charge generation rate which is proportional to the irradiation power (P) and electron and hole diffusion lengths, respectively.[50] Therefore, with the help of these both equations, we get equation expressed as

$$\mu \propto (R/\sqrt{\tau})^2$$

Figure 3f shows $R/\sqrt{\tau}$ as a function of irradiation power, which suggests that there is no change in carrier mobility under different irradiation power.

Next, the effect of different temperatures on the performance of a PD was studied. First, we collected the I–V characteristics under darkness and within a wide temperature range from 303 to 353 K. As shown in Figure S13, the dark current of the PD increases with increasing of the temperature. The high temperature activates the defect and ions, which improves the conductivity of the SC as previously reported.[13,14,28] The temperature dependence of photocurrent as a function of bias is shown in Figure 4a. The photocurrent of the PD increases up to 313 K and then decreases with increasing of the temperature for all irradiation intensities. This behavior can be correlated with the passivation effect by carrier-trapping and/or temperature-activated ions at the defect states.[35] It was reported that ion migration may enhance with increasing of the temperature.[14,51] Initially, the temperature-activated ion migration passivates the surface of the $MAPbBr_3$ SC and reduces the defect states. These effects improve the performance of the PD by reducing the charge recombination. For the temperature higher than 313 K, the density of temperature-activated ions increases, leading to ion

https://doi.org/10.1021/acsphotonics.3c00033
ACS Photonics 2023, 10, 1424−1433

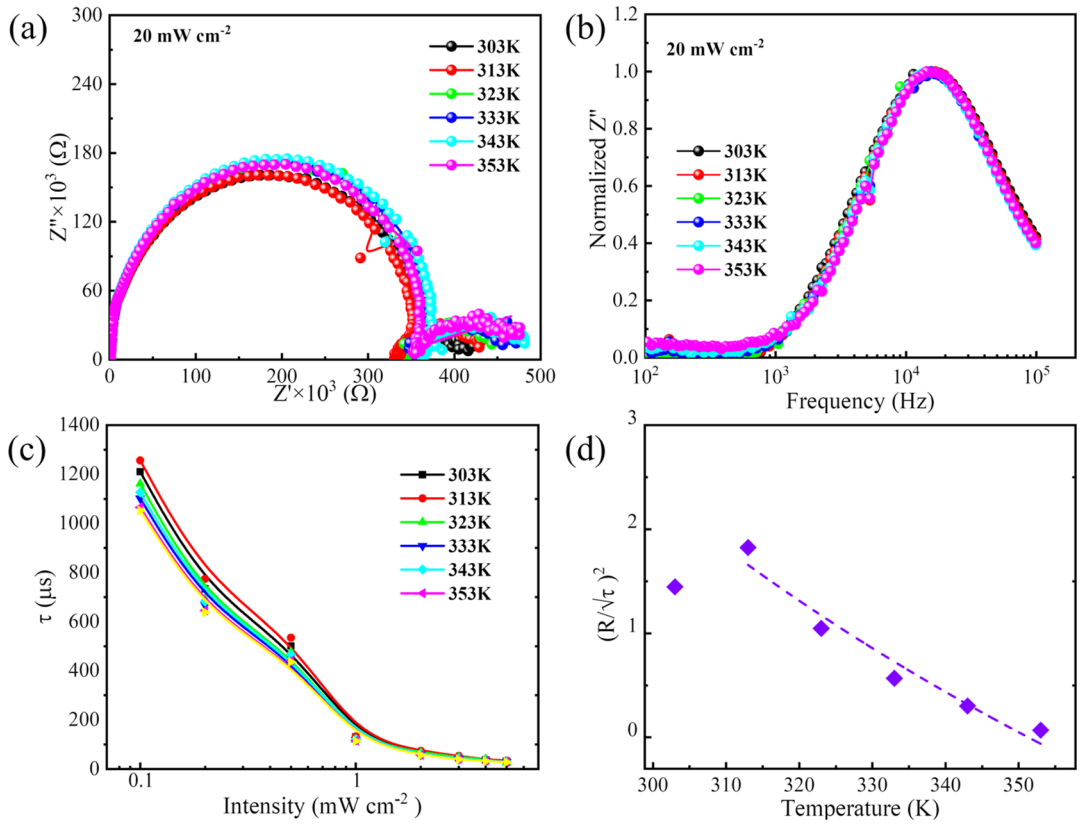

Figure 5. (a) Nyquist spectra and (b) normalized imaginary part (Z'') of IS spectra versus frequency under various temperature at 20 mW cm^{-2} irradiation power. (c) Temperature-dependent carrier recombination lifetime under various irradiation intensities. (d) $(R/\sqrt{\tau})^2$, extracted from temperature-dependent IS and photodetectivity and fitted by a power law at 20 mW cm^{-2} irradiation power.

accumulation and charge trapping that introduce dominating scattering of impurities and phonons over the recombination mechanism (vide infra).

The device parameters were determined for every temperature and plotted against the irradiation power of incident light (Figure 4b–d). The maximum values of R, D^*, and EQE are estimated to be 2.18 A W^{-1}, 1.81 × 10^{12} Jones, and 569% at 313 K and under 0.1 mW cm^{-2} blue light at a fixed bias voltage of 2 V. Encouragingly, the PD still operates at 353 K, and the calculated R remains 30% of its original value (R = 0.57 A W^{-1}) (Figure 4b). We continuously kept the PD at 353 K for 5 h and found that R reduced only by 5%. When we cooled down the PD to room temperature, the calculated R returns to 97% of its initial value (Figure S14). Therefore, the decrease in R within the probed temperature range is not related to the degradation of the perovskite structure.

To put light on understanding the temperature dependence operational behavior, the temperature-dependent IS was carried out in the frequencies ranging from 100 mHz to 1 MHz under 20 mW cm^{-2} and at 2 V bias condition (Figure 5a). We observed an increase in both the high- and low-frequency semicircle radius of the IS spectra with increasing of the temperature. These results suggest that the charge transport resistance and/or charge recombination resistance increases with temperature. To check which resistance process dominates at the probed temperatures, a normalized imaginary part of IS vs frequency as a function of temperature under a constant irradiance power was plotted (Figure 5b). In contrast to the similar plot but shown as a function of different irradiation powers (Figure 3d), the shift in resonance frequency is not observed with increasing of the temperature. Consequently, the effect of temperature on the change in the carrier recombination lifetime of the PD is minor (Figure 5c) and is similar for other irradiation intensities (Figure S15). Therefore, the reduced photoresponsivity with temperature cannot be explained by the recombination mechanism.

The low-frequency semicircle, which is related to the slow process of ion migration, increases with temperature, suggesting the increase of ion accumulation between the Pt/$MAPbBr_3$ interface. On the other hand, the charge carrier mobility of the perovskite SC is typically controlled by scattering of impurities and phonons (lattice vibrations).[52,53] In detail, the elastic and inelastic scattering of acoustic phonons leads to a power law of $\mu \propto T^{-3/2}$ and $T^{-1/2}$, respectively. However, scattering of impurities or ions leads to a power law of $\mu \propto T^{+3/2}$. According to the recent reports,[52,53] the optical phonons play a major role in charge carrier mobility. The value of the exponent depends on the measurement procedure and structure of the perovskite (i.e., orthorhombic, tetragonal, and cubic) and can be varied from −0.6 to −2.5.[52−56] As we previously discussed carrier mobility with equation $\mu \propto (R/\sqrt{\tau})^2$, $(R/\sqrt{\tau})^2$ as a function of temperature at different irradiation powers was plotted and is shown in Figure 5d. The exponent value was determined to equal −1.79 ± 0.3 for cubic $MAPbBr_3$ under 20 mW cm^{-2}, suggesting that the decrease in the photoresponse of a PD at high temperatures (above 313 K) is due to the reduced carrier mobility caused by the scattering mechanism. The exponent value changes slowly with changing of the light intensity and varied from ∼1.65 to ∼1.85 for lower and higher intensities,

https://doi.org/10.1021/acsphotonics.3c00033
ACS Photonics 2023, 10, 1424−1433

respectively (Figure S16). These results indicate that the increase in scattering of ions with increasing of the intensity leads to the variation of the exponent value, which is consistent with our previous section findings. In addition, as reported by Mannino et al.,[57] the band gap of $MAPbBr_3$ increases with temperature, which may reduce the charge generation of the PD at high temperature. The decrease in the performance of our PD above 313 K can be summarized as a combined effect of the ion accumulation (higher ion migration at elevated temperature), reduced carrier mobility (increasing scattering at higher temperature) and charge generation (increase in band gap with temperature), and increase in dark current.

3. CONCLUSIONS

In this work, we investigated the effect of different light intensities and temperatures on the photodetection properties of the $MAPbBr_3$ SC-based PD. Based on the calculated output parameters, we first demonstrated that the $MAPbBr_3$ SC-based PD with the Pt electrode shows better performance than the PD with the Au electrode due to better SBH alignment and thus effective charge extraction. Next, we studied the effect of Pt electrode spacing on the performance of the $MAPbBr_3$ SC-based PD and determined the best performing device with a Pt electrode spacing of 150 μm. This device exhibited the R of 1.99 A W^{-1}, D^* of 5.09×10^{12} Jones, and EQE of 553% under 0.1 mW cm^{-2} blue light and 2 V bias, which are comparable with the previously reported studies on $MAPbBr_3$ SC-based PDs (Table S2). For the systematic understanding of the effect of light and temperature on the photodetection performance, the PD was examined by IS under irradiation power densities ranging from 1 to 50 mW cm^{-2} and temperatures ranging from 303 to 353 K. The charge recombination plays a significant role in the intensity dependence of PD performance, leading to a decrease in performance parameters (R, D^*, and EQE) with increasing light intensity. On the other hand, the negligible change of carrier lifetime at the probed temperature range reveals that the decreased performance of the PD for the temperatures above 313 K is not related to the charge recombination. Rather, it can be attributed to the combined effect of the change in ion accumulation, different types of scattering, conductivity, and band gap with increasing of the temperature. Notably, the PD still operates at 353 K, showing an R value of 0.58 A W^{-1} under 0.1 mW cm^{-2} blue light and 2 V bias. This study provides a basic insight into the relationship between the light intensity and temperature dependence performance of the $MAPbBr_3$ SC-based PD with the carrier recombination, ion migration, different types of scattering, and conductivity, which could be helpful for the further advancement of photoelectronic devices.

4. EXPERIMENTAL SECTION

4.1. Synthesis and Characterization of $MAPbBr_3$ SCs. $MAPbBr_3$ SCs were synthesized using the inverse temperature crystallization (ITC) method. 1.2 M $MAPbBr_3$ solution was prepared by dissolving the equimolar amounts of $PbBr_2$ (1.321 g, Sigma-Aldrich) and MABr (0.403 g, Sigma-Aldrich) in 3 mL of anhydrous DMF and stirring the solution at room temperature for 24 h. Next, the clear solution was filtered using a 0.22 μm PTFE filter, and 2 mL of each filtered transparent solution was sealed in bottles and kept at 80 °C for 4 h. The formed crystals were washed by isopropyl alcohol, then dried at 100 °C for 15 min, and stored in a humid-free chamber.

The X-ray powder diffraction measurements were carried out using an Empyrean diffractometer (PANalytical) equipped with a copper lamp (40 kV, 40 mA). The pXRD patterns were recorded for finely ground crystals over a 2θ range of 10−50° without rotating the sample using a low background Si sample holder.

4.2. Fabrication and Characterizations of the Pt/$MAPbBr_3$/Pt and Au/$MAPbBr_3$/Au PDs. 100 nm-thick platinum (Pt) and gold (Au) electrodes were deposited using a designed mask with different micrometer channels by a sputtered magnetron (Leica EM MED020) on (100) facets of the SCs. To perform SCLC measurement, Au and Pt electrodes were deposited on both sides of the $MAPbBr_3$ SC. All dark current−voltage and PD response measurements were performed on a LASC probe station connected to a Bio-Logic SP-150e potentiostat at a scan rate of 100 mV s^{-1}. The illumination power of blue LED with a wavelength of 448 nm (Luxeonstar) was optimized with the help of a spectrometer Thorlabs GmbH., PM 100D.

■ ASSOCIATED CONTENT

Supporting Information

The Supporting Information is available free of charge at https://pubs.acs.org/doi/10.1021/acsphotonics.3c00033.

Powder X-ray diffraction patterns; intensity-dependent transient photoresponse; light current−voltage characteristics; dark current−voltage characteristics; functional stability of the $MAPbBr_3$ SC-based PD; relationship between photocurrent density and irradiation power; Nyquist spectra; complex impedance part as a function of frequency and light intensity; and temperature-dependent dark current−voltage responses (PDF)

■ AUTHOR INFORMATION

Corresponding Author

Daniel Prochowicz − *Institute of Physical Chemistry, Polish Academy of Sciences, 01-224 Warsaw, Poland;* orcid.org/0000-0002-5003-5637; Email: dprochowicz@ichf.edu.pl

Authors

Apurba Mahapatra − *Institute of Physical Chemistry, Polish Academy of Sciences, 01-224 Warsaw, Poland;* orcid.org/0000-0003-0799-9470

Vishnu Anilkumar − *Institute of Physical Chemistry, Polish Academy of Sciences, 01-224 Warsaw, Poland;* orcid.org/0000-0002-7914-1302

Rohit D. Chavan − *Institute of Physical Chemistry, Polish Academy of Sciences, 01-224 Warsaw, Poland;* orcid.org/0000-0001-9254-5048

Pankaj Yadav − *Department of Solar Energy, School of Energy Technology, Pandit Deendayal Energy University, 382 007 Gandhinagar, Gujarat, India;* orcid.org/0000-0002-1858-8397

Complete contact information is available at: https://pubs.acs.org/10.1021/acsphotonics.3c00033

Funding

D.P., A.M., and V.A. acknowledge the National Science Centre (grant OPUS-20, no. 2020/39/B/ST5/01497) for financial support.

Notes

The authors declare no competing financial interest.

REFERENCES

(1) García De Arquer, F. P.; Armin, A.; Meredith, P.; Sargent, E. H. Solution-Processed Semiconductors for next-Generation Photodetectors. *Nat. Rev. Mater.* **2017**, *2*, 16100.

(2) Cao, F.; Xu, X.; Yu, D.; Zeng, H. Lead-Free Halide Perovskite Photodetectors Spanning from near-Infrared to X-Ray Range: A Review. *Nanophotonics* **2021**, *10*, 2221−2247.

(3) Wang, H.; Kim, D. H. Perovskite-Based Photodetectors: Materials and Devices. *Chem. Soc. Rev.* **2017**, *46*, 5204−5236.

(4) Xu, Y.; Lin, Q. Photodetectors Based on Solution-Processable Semiconductors: Recent Advances and Perspectives. *Appl. Phys. Rev.* **2020**, *7*, 011315.

(5) Jansen-van Vuuren, R. D.; Armin, A.; Pandey, A. K.; Burn, P. L.; Meredith, P. Organic Photodiodes: The Future of Full Color Detection and Image Sensing. *Adv. Mater.* **2016**, *28*, 4766−4802.

(6) Li, G.; Wang, Y.; Huang, L.; Sun, W. Research Progress of High-Sensitivity Perovskite Photodetectors: A Review of Photodetectors: Noise, Structure, and Materials. *ACS Appl. Electron. Mater.* **2022**, *4*, 1485−1505.

(7) Manser, J. S.; Christians, J. A.; Kamat, P. V. Intriguing Optoelectronic Properties of Metal Halide Perovskites. *Chem. Rev.* **2016**, *116*, 12956−13008.

(8) Miao, J.; Zhang, F. Recent Progress on Highly Sensitive Perovskite Photodetectors. *J. Mater. Chem. C* **2019**, *7*, 1741−1791.

(9) Ahmadi, M.; Wu, T.; Hu, B. A Review on Organic−Inorganic Halide Perovskite Photodetectors: Device Engineering and Fundamental Physics. *Adv. Mater.* **2017**, *29*, 1605242.

(10) Dunlap-Shohl, W. A.; Zhou, Y.; Padture, N. P.; Mitzi, D. B. Synthetic Approaches for Halide Perovskite Thin Films. *Chem. Rev.* **2019**, *119*, 3193−3295.

(11) Trivedi, S.; Prochowicz, D.; Parikh, N.; Mahapatra, A.; Pandey, M. K.; Kalam, A.; Tavakoli, M. M.; Yadav, P. Recent Progress in Growth of Single-Crystal Perovskites for Photovoltaic Applications. *ACS Omega* **2021**, *6*, 1030−1042.

(12) Dong, Q.; Fang, Y.; Shao, Y.; Mulligan, P.; Qiu, J.; Cao, L.; Huang, J. Electron-Hole Diffusion Lengths > 175 μm in Solution-Grown $CH_3NH_3PbI_3$ Single Crystals. *Science* **2015**, *347*, 967−970.

(13) Mahapatra, A.; Parikh, N.; Kumari, H.; Pandey, M. K.; Kumar, M.; Prochowicz, D.; Kalam, A.; Tavakoli, M. M.; Yadav, P. Reducing Ion Migration in Methylammonium Lead Tri-Bromide Single Crystal via Lead Sulfate Passivation. *J. Appl. Phys.* **2020**, *127*, 185501.

(14) Mahapatra, A.; Prochowicz, D.; Kruszyńska, J.; Satapathi, S.; Akin, S.; Kumari, H.; Kumar, P.; Fazel, Z.; Tavakoli, M. M.; Yadav, P. Effect of Bromine Doping on the Charge Transfer, Ion Migration and Stability of the Single Crystalline $MAPb(Br_xI_{1-x})_3$ Photodetector. *J. Mater. Chem. C* **2021**, *9*, 15189−15200.

(15) Zhou, J.; Huang, J. Photodetectors Based on Organic−Inorganic Hybrid Lead Halide Perovskites. *Adv. Sci.* **2018**, *5*, 1700256.

(16) Guo, W.; Xu, H.; Ma, Y.; Liu, Y.; Wang, B.; Tang, L.; Hua, L.; Luo, J.; Sun, Z. The Unprecedented Highest-Layer-Number Ferroelectric Semiconductor of 2D Homologous Single-Phase Perovskites Tailored by Regulating Thickness of Inorganic Frameworks. *Adv. Funct. Mater.* **2022**, *32*, 2207854.

(17) Lu, L.; Weng, W.; Ma, Y.; Liu, Y.; Han, S.; Liu, X.; Xu, H.; Lin, W.; Sun, Z.; Luo, J. Anisotropy in a 2D Perovskite Ferroelectric Drives Self-Powered Polarization-Sensitive Photoresponse for Ultraviolet Solar-Blind Polarized-Light Detection. *Angew. Chem., Int. Ed.* **2022**, *61*, No. e202205030.

(18) Chen, Y.; Gao, C.; Yang, T.; Li, W.; Xu, H.; Sun, Z. Research Advances of Ferroelectric Semiconductors of 2D Hybrid Perovskites toward Photoelectronic Applications. *Chin. J. Struct. Chem.* **2022**, *41*, 2204001.

(19) Guo, W.; Chen, H.; Liu, X.; Ma, Y.; Wang, J.; Liu, Y.; Han, S.; Xu, H.; Luo, J.; Sun, Z. Rational alloying of secondary and aromatic ammonium cations in a metal-halide perovskite toward crystal-array photodetection. *Sci. China Mater.* **2021**, *65*, 179−185.

(20) Li, C.; Wang, H.; Wang, F.; Li, T.; Xu, M.; Wang, H.; Wang, Z.; Zhan, X.; Hu, W.; Shen, L. Ultrafast and Broadband Photodetectors Based on a Perovskite/Organic Bulk Heterojunction for Large-Dynamic-Range Imaging. *Light: Sci. Appl.* **2020**, *9*, 31.

(21) Liu, Y.; Zhang, Y.; Zhao, K.; Yang, Z.; Feng, J.; Zhang, X.; Wang, K.; Meng, L.; Ye, H.; Liu, M.; Liu, S. F. 1300 mm^2 Ultrahigh-Performance Digital Imaging Assembly Using High-Quality Perovskite Single Crystals. *Adv. Mater.* **2018**, *30*, 1707314.

(22) Zuo, Z.; Ding, J.; Zhao, Y.; Du, S.; Li, Y.; Zhan, X.; Cui, H. Enhanced Optoelectronic Performance on the (110) Lattice Plane of an $MAPbBr_3$ Single Crystal. *J. Phys. Chem. Lett.* **2017**, *8*, 684−689.

(23) Zhang, Z.; Chen, K.; Xia, W.; Zuo, Z. $MAPbBr_3$ Single Crystal Based Metal-Semiconductor-Metal Photodetector Enhanced by Localized Surface Plasmon. *Mater. Res. Express* **2020**, *7*, 125902.

(24) Armaroli, G.; Ferlauto, L.; Lédée, F.; Lini, M.; Ciavatti, A.; Kovtun, A.; Borgatti, F.; Calabrese, G.; Milita, S.; Fraboni, B.; Cavalcoli, D. X-Ray-Induced Modification of the Photophysical Properties of $MAPbBr_3$ Single Crystals. *ACS Appl. Mater. Interfaces* **2021**, *13*, 58301−58308.

(25) Liu, Y.; Zhang, Y.; Yang, Z.; Feng, J.; Xu, Z.; Li, Q.; Hu, M.; Ye, H.; Zhang, X.; Liu, M.; Zhao, K.; Liu, S. Low-Temperature-Gradient Crystallization for Multi-Inch High-Quality Perovskite Single Crystals for Record Performance Photodetectors. *Mater. Today* **2019**, *22*, 67−75.

(26) Cho, Y.; Jung, H. R.; Kim, Y. S.; Kim, Y.; Park, J.; Yoon, S.; Lee, Y.; Cheon, M.; Jeong, S. Y.; Jo, W. High Speed Growth of $MAPbBr_3$ Single Crystals via Low-Temperature Inverting Solubility: Enhancement of Mobility and Trap Density for Photodetector Applications. *Nanoscale* **2021**, *13*, 8275−8282.

(27) Jing, L.; Cheng, X.; Yuan, Y.; Du, S.; Ding, J.; Sun, H.; Zhan, X.; Zhou, T. Design Growth of Triangular Pyramid $MAPbBr_3$ Single Crystal and Its Photoelectric Anisotropy between (100) and (111) Facets. *J. Phys. Chem. C* **2019**, *123*, 10826−10830.

(28) Kalam, A.; Runjhun, R.; Mahapatra, A.; Tavakoli, M. M.; Trivedi, S.; Tavakoli Dastjerdi, H.; Kumar, P.; Lewiński, J.; Pandey, M.; Prochowicz, D.; Yadav, P. Interpretation of Resistance, Capacitance, Defect Density, and Activation Energy Levels in Single-Crystalline $MAPbI_3$. *J. Phys. Chem. C* **2020**, *124*, 3496−3502.

(29) Mahapatra, A.; Runjhun, R.; Nawrocki, J.; Lewiński, J.; Kalam, A.; Kumar, P.; Trivedi, S.; Tavakoli, M. M.; Prochowicz, D.; Yadav, P. Elucidation of the Role of Guanidinium Incorporation in Single-Crystalline $MAPbI_3$ Perovskite on Ion Migration and Activation Energy. *Phys. Chem. Chem. Phys.* **2020**, *22*, 11467−11473.

(30) Cui, X.; Yuan, S.; Zhang, H.; Zhang, X.; Wang, P.; Tu, L.; Sun, Z.; Wang, J.; Zhan, Y.; Zheng, L. Temperature-Dependent Electronic Properties of Inorganic-Organic Hybrid Halide Perovskite ($CH_3NH_3PbBr_3$) Single Crystal. *Appl. Phys. Lett.* **2017**, *111*, 233302.

(31) Zhou, J.; Lei, N.; Zhou, H.; Zhang, Y.; Tang, Z.; Jiang, L. Understanding the Temperature-Dependent Charge Transport, Structural Variation and Photoluminescent Properties in Methylammonium Lead Halide Perovskite Single Crystals. *J. Mater. Chem. C* **2018**, *6*, 6556−6564.

(32) Lian, Z.; Yan, Q.; Lv, Q.; Wang, Y.; Liu, L.; Zhang, L.; Pan, S.; Li, Q.; Wang, L.; Sun, J. L. High-Performance Planar-Type Photodetector on (100) Facet of $MAPbI_3$ Single Crystal. *Sci. Rep.* **2015**, *5*, 16563.

(33) Mahapatra, A.; Chavan, R. D.; Tavakoli, M. M.; Kumar, P.; Kalam, A.; Prochowicz, D.; Yadav, P. Revealing the Variation of Photodetectivity in $MAPbI_3$ and $MAPb(I_{0.88}Br_{0.12})_3$ Single Crystal Based Photodetectors Under Electrical Poling-Induced Polarization. *J. Phys. Chem. C* **2022**, *126*, 13458−13466.

(34) Gavranovic, S.; Pospisil, J.; Zmeskal, O.; Novak, V.; Vanysek, P.; Castkova, K.; Cihlar, J.; Weiter, M. Electrode Spacing as a Determinant of the Output Performance of Planar-Type Photodetectors Based on Methylammonium Lead Bromide Perovskite Single Crystals. *ACS Appl. Mater. Interfaces* **2022**, *14*, 20159−20167.

(35) Cho, Y.; Jung, H. R.; Jo, W. Photo-Induced Defects in $MAPbBr_3$ Single Crystals. *J. Phys.: Energy* **2021**, *3*, 044005.

https://doi.org/10.1021/acsphotonics.3c00033
ACS Photonics 2023, 10, 1424−1433

(36) Khanam, S. J.; Parikh, N.; Satapathi, S.; Kalam, A.; Banavoth, M.; Yadav, P. Role of Heterocyclic Organic Compounds on the Optoelectronic Properties of Halide Perovskite Single Crystals. *ACS Appl. Energy Mater.* **2022**, *5*, 14732−14738.
(37) Wang, Y.; Zhang, Y.; Liu, Y.; Pang, T.; Hu, Z.; Zhu, Y.; Luan, S.; Jia, R. Temperature-Dependence Studies of Organolead Halide Perovskite-Based Metal/Semiconductor/Metal Photodetectors. *RSC Adv.* **2017**, *7*, 20206−20211.
(38) Yun, Y.; Han, G. S.; Park, G. N.; Kim, J.; Park, J.; Vidyasagar, D.; Jung, J.; Choi, W. C.; Choi, Y. J.; Heo, K.; Kang, J.; Park, J.-S.; et al. A Wide Bandgap Halide Perovskite Based Self-Powered Blue Photodetector with 84.9% of External Quantum Efficiency. *Adv. Mater.* **2022**, *34*, 2206932.
(39) Chu, Y.; Chen, Y.; Zhou, J.; Zhou, B.; Huang, J. Efficient and Stable Perovskite Photodetectors Based on Thiocyanate-Assisted Film Formation. *ACS Appl. Mater. Interfaces* **2019**, *11*, 14510−14514.
(40) Fang, H.; Hu, W. Photogating in Low Dimensional Photodetectors. *Adv. Sci.* **2017**, *4*, 1700323.
(41) Dualeh, A.; Moehl, T.; Tétreault, N.; Teuscher, J.; Gao, P.; Nazeeruddin, M. K.; Grätzel, M. Impedance Spectroscopic Analysis of Lead Iodide Perovskite-Sensitized Solid-State Solar Cells. *ACS Nano* **2014**, *8*, 362−373.
(42) Yadav, P.; Parikh, N.; Prochowicz, D.; Kalam, A.; Tavakoli, M. M.; Akin, S.; Banavoth, M. Probing the Surface and Bulk Electrical Response of $MAPbBr_3$ Single Crystals. *J. Phys. Chem. C* **2022**, *126*, 12399−12404.
(43) Prochowicz, D.; Trivedi, S.; Parikh, N.; Saliba, M.; Kalam, A.; Mahdi Tavakoli, M.; Yadav, P. In the Quest of Low-Frequency Impedance Spectra of Efficient Perovskite Solar Cells. *Energy Technol.* **2021**, *9*, 2100229.
(44) Mahapatra, A.; Parikh, N.; Kumar, P.; Kumar, M.; Prochowicz, D.; Kalam, A.; Tavakoli, M. M.; Yadav, P. Changes in the Electrical Characteristics of Perovskite Solar Cells with Aging Time. *Molecules* **2020**, *25*, 2299.
(45) Solanki, A.; Guerrero, A.; Zhang, Q.; Bisquert, J.; Sum, T. C. Interfacial Mechanism for Efficient Resistive Switching in Ruddlesden−Popper Perovskites for Non-Volatile Memories. *J. Phys. Chem. Lett.* **2020**, *11*, 463−470.
(46) Guerrero, A.; Garcia-Belmonte, G.; Mora-Sero, I.; Bisquert, J.; Kang, Y. S.; Jacobsson, T. J.; Correa-Baena, J.-P.; Hagfeldt, A. Properties of Contact and Bulk Impedances in Hybrid Lead Halide Perovskite Solar Cells Including Inductive Loop Elements. *J. Phys. Chem. C* **2016**, *120*, 8023−8032.
(47) Meggiolaro, D.; Mosconi, E.; De Angelis, F. Formation of Surface Defects Dominates Ion Migration in Lead-Halide Perovskites. *ACS Energy Lett.* **2019**, *4*, 779−785.
(48) Zhao, Y.-C. C.; Zhou, W.-K. K.; Zhou, X.; Liu, K.-H. H.; Yu, D.-P. P.; Zhao, Q. Quantification of Light-Enhanced Ionic Transport in Lead Iodide Perovskite Thin Films and Its Solar Cell Applications. *Light: Sci. Appl.* **2016**, *6*, No. e16243.
(49) Hodes, G.; Kamat, P. V. Understanding the Implication of Carrier Diffusion Length in Photovoltaic Cells. *J. Phys. Chem. Lett.* **2015**, *6*, 4090−4092.
(50) Green, M. A. Solar Cells—Operating Principles, Technology and System Applications. *Sol. Energy* **1982**, *28*, 447.
(51) Tailor, N. K.; Mahapatra, A.; Kalam, A.; Pandey, M.; Yadav, P.; Satapathi, S. Influence of the A-Site Cation on Hysteresis and Ion Migration in Lead-Free Perovskite Single Crystals. *Phys. Rev. Mater.* **2022**, *6*, 045401.
(52) Shrestha, S.; Matt, G. J.; Osvet, A.; Niesner, D.; Hock, R.; Brabec, C. J. Assessing Temperature Dependence of Drift Mobility in Methylammonium Lead Iodide Perovskite Single Crystals. *J. Phys. Chem. C* **2018**, *122*, 5935−5939.
(53) Biewald, A.; Giesbrecht, N.; Bein, T.; Docampo, P.; Hartschuh, A.; Ciesielski, R. Temperature-Dependent Ambipolar Charge Carrier Mobility in Large-Crystal Hybrid Halide Perovskite Thin Films. *ACS Appl. Mater. Interfaces* **2019**, *11*, 20838−20844.
(54) Karakus, M.; Jensen, S. A.; D'Angelo, F.; Turchinovich, D.; Bonn, M.; Cánovas, E. Phonon−Electron Scattering Limits Free Charge Mobility in Methylammonium Lead Iodide Perovskites. *J. Phys. Chem. Lett.* **2015**, *6*, 4991−4996.
(55) Oga, H.; Saeki, A.; Ogomi, Y.; Hayase, S.; Seki, S. Improved Understanding of the Electronic and Energetic Landscapes of Perovskite Solar Cells: High Local Charge Carrier Mobility, Reduced Recombination, and Extremely Shallow Traps. *J. Am. Chem. Soc.* **2014**, *136*, 13818−13825.
(56) Milot, R. L.; Eperon, G. E.; Snaith, H. J.; Johnston, M. B.; Herz, L. M. Temperature-Dependent Charge-Carrier Dynamics in $CH_3NH_3PbI_3$ Perovskite Thin Films. *Adv. Funct. Mater.* **2015**, *25*, 6218−6227.
(57) Mannino, G.; Deretzis, I.; Smecca, E.; La Magna, A.; Alberti, A.; Ceratti, D.; Cahen, D. Temperature-Dependent Optical Band Gap in $CsPbBr_3$, $MAPbBr_3$, and $FAPbBr_3$ Single Crystals. *J. Phys. Chem. Lett.* **2020**, *11*, 2490−2496.

https://doi.org/10.1021/acsphotonics.3c00033
ACS Photonics 2023, 10, 1424−1433